Eur. Phys. J. C 28, 79–95 (2003)
Digital Object Identifier (DOI) 10.1140/epjc/s2003-01132-6

THE EUROPEAN PHYSICAL JOURNAL C

The charge and matter radial distributions of heavy-light mesons calculated on a lattice with dynamical fermions

The UKQCD Collaboration

A.M. Green[1,a], J. Koponen[1,b], P. Pennanen[1,c], C. Michael[2,d]

[1] Department of Physical Sciences and Helsinki Institute of Physics, P.O. Box 64, 00014 University of Helsinki, Finland
[2] Department of Mathematical Sciences, University of Liverpool, L69 3BX, UK

Received: 2 September 2002 / Revised version: 9 December 2002 /
Published online: 3 March 2003 –

Abstract. A knowledge of the radial distributions of quarks inside hadrons could lead to a better understanding of the QCD description of these hadrons and possibly suggest forms for phenomenological models. As a step in this direction, in an earlier work, the charge (vector) and matter (scalar) radial distributions of heavy-light mesons were measured in the quenched approximation on a $16^3 \times 24$ lattice with a lattice spacing of $a \approx 0.17$ fm, and a hopping parameter corresponding to a light quark mass about that of the strange quark. Here several improvements are now made: 1) The configurations are generated using dynamical fermions with $a \approx 0.14$ fm; 2) Many more gauge configurations are included; 3) The distributions at many off-axis, in addition to on-axis, points are measured; 4) The data analysis is much more complete. In particular, distributions involving excited states are extracted. The exponential decay of the charge and matter distributions can be described by mesons of mass 0.9±0.1 and 1.5±0.1 GeV respectively – values that are consistent with those of vector and scalar $q\bar{q}$-states calculated *directly* with the same lattice parameters.

1 Introduction

In few- and many-body systems radial and momentum distributions often play an important role. For atomic and nuclear systems these distributions are, in many cases, calculated from a differential equation using an effective interparticle potential, where both the equation and potential have some justification. However, for quark-gluon systems this approach is thought not to be applicable, even though the basic interaction – that of QCD – is exact and well known. Therefore, if – for example – transition rates between states in a heavy-light meson ($Q\bar{q}$) are calculated, then the necessary radial wavefunctions are simply taken to have some convenient form, as in [1], or are calculated with a differential equation and interquark interaction that are not well justified. It is an unusual situation, where one of the most fundamental systems, the hydrogen atom of quark physics, has interparticle correlations that are little understood.

In an attempt to remedy partially this problem, the authors in [2] *measured* the charge and matter distributions in a heavy-light meson. More explicitly, the heavy-light meson was simplified to being an infinitely heavy quark (Q) and an antiquark ($\bar{q}$) with a mass approximately equal to that of the strange quark. The physical meson nearest to this idealised meson is the $B_s(5.37$ GeV). Reference [2] was essentially a pilot calculation to test the feasibility of such distribution measurements and its successful outcome encouraged the authors to continue this line of research. In this paper, the same correlations are measured but with several major improvements compared with the earlier study:

1) The gauge configurations are now calculated using two flavors of dynamical fermion and not in the quenched approximation as before. The actual parameters are those in [3], namely, $\beta = 5.2$, $C_{\rm SW} = 1.76$ for the clover action, $a \approx 0.14$ fm for the lattice spacing, $\kappa = 0.1395$ for the hopping parameter and $M_{\rm PS}/M_V = 0.72$ for the pseudoscalar meson/vector meson mass ratio, which corresponds to a quark mass somewhat heavier than the strange quark mass – $M_{\rm PS}/M_V = 0.682$ being the ratio corresponding to exactly the strange quark mass [4]. In comparison, the parameters for the quenched work of [2] were $\beta = 5.7$, $C_{\rm SW} = 1.57$, $a \approx 0.17$ fm, $\kappa = 0.14077$ and $M_{\rm PS}/M_{\rm V} = 0.65$, corresponding to [5] a value of $m_{\bar{q}} = 0.91(2)m_{\rm s}$. The spatial lattice size is 2.24 fm (compared to 2.72 fm in the previous quenched calculation).

2) Many more gauge configurations are generated – 78 with dynamical fermions compared with the earlier 20 quenched configurations.

[a] e-mail: anthony.green@helsinki.fi
[b] e-mail: jonna.koponen@helsinki.fi
[c] e-mail: petrus@leiki.fi
[d] e-mail: cmi@liv.ac.uk

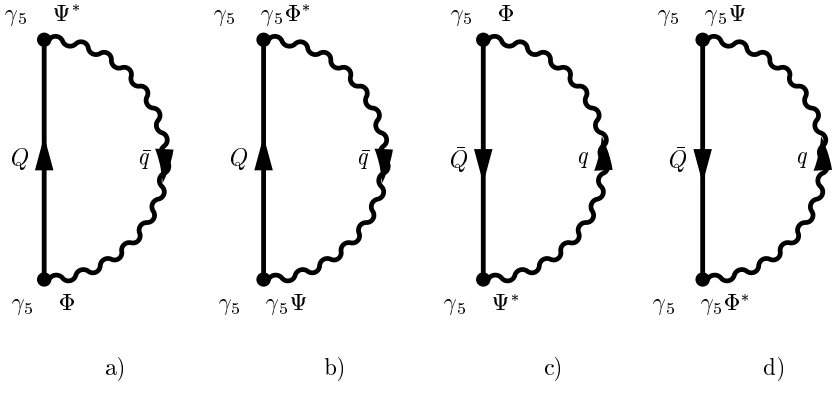

Fig. 1a–d. The four contributions to the two-point correlation function C_2

3) Previously the densities were measured only at the 7 on-axis points $r = 0, 1, \ldots, 6$. Now the densities at 20 points are measured – the same 7 on-axis with the addition of 13 off-axis points. This permits a potentially much more detailed mapping of the density profiles. Furthermore, it opens up the possibility of testing the rotational invariance of these profiles by comparing them at $r = 5$ with that at $(x = 3, y = 4)$ and also $r = 3$ with $(x = 2, y = 2, z = 1)$. This symbolic notation for an off-axis point will be used throughout the article. In practice, it includes the 8 possibilities $(x = \pm 3, y = \pm 4)$ and $(x = \pm 4, y = \pm 3)$, so that when combined with the directions along the 3 axes, this makes 24 independent measurements for each symbolic (x, y), when $x \neq y$. In contrast, the on-axis cases have only 6 independent measurements for each r. This will be seen to improve significantly the statistics for the off-axis points compared with their neighboring on-axis points. This is in spite of the fact that an off-axis point requires a longer string of latticized links, so that – being guided by strong coupling arguments – it should be more difficult to measure.

4) Since the work in [2], the methods and our understanding of the data analysis have been developed. In particular, the interesting off-diagonal density terms are always allowed to vary and are no longer fixed to zero as was sometimes the case earlier. This now gives a better estimate of excited state effects. Also for the radial dependence of the density $x^{\alpha\beta}(r)$, the use of a separable form $y_\alpha(r)y_\beta(r)$ is also employed. Here α, β are state indices with $\alpha = 1$ being the ground state. This separable form is found to have some interesting features not found in the non-separable approach. Furthermore, *if* the densities were to be interpreted in terms of underlying wavefunctions $\psi_\alpha(r)$, then the separable form $x^{\alpha\beta}(r) = \psi_\alpha(r)\psi_\beta(r)$ would be perfectly natural. However, it should be emphasised that such an interpretation can only have a phenomenological justification.

In Sect. 2 the two- and three-point correlation functions needed to extract the densities are briefly discussed – the reader being referred to [2] for more details. In Sect. 3 the methods for analysing the basic lattice data are described. This results in values for the ground and some excited state energies and, in addition, radial distributions of the charge (vector) and matter (scalar) densities for these

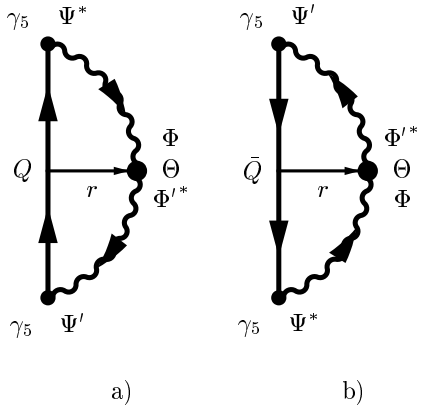

Fig. 2a,b. The two contributions to the three-point correlation function C_3

states are extracted. In Sect. 4 these radial distributions are parametrized in terms of latticized forms of Yukawa, exponential and gaussian functions. In Sect. 5 a summary and some conclusions are made.

2 The correlation functions C_2 and $C_3(r)$

In this work the basic entities are the two- and three-point correlations C_2 and C_3, both of which are needed for measuring radial distributions. These are depicted in Figs. 1 and 2 and are seen to be constructed from essentially two quantities – the heavy (static)-quark propagator G_Q and the light-quark propagator G_q.

As discussed in detail in [2], when the heavy-quark propagates from site $(\mathbf{x}, t)$ to site $(\mathbf{x}', t + T)$, G_Q can be expressed as

$$G_Q(\mathbf{x}, t; \mathbf{x}', t + T) = \frac{1}{2}(1 + \gamma_4)U^Q(\mathbf{x}, t, T)\delta_{\mathbf{x},\mathbf{x}'}, \qquad (1)$$

where $U^Q(\mathbf{x}, t, T) = \prod_{i=0}^{T-1} U_4(\mathbf{x}, t + i)$ is the gauge link product in the time direction. On the other hand, as the light-quark propagates from site i to site j, it can be schematically expressed as [5]

$$G_q = G_{ji} = Q_{ji}^{-1} = \langle (Q_{ik}\phi_k)^*\phi_j \rangle = \langle \psi_i^*\phi_j \rangle. \qquad (2)$$

or as

$$G'_q = G'_{ji} = \gamma_5\langle(Q_{jk}\phi_k)\phi_i^*\rangle\gamma_5 = \gamma_5\langle\psi_j\phi_i^*\rangle\gamma_5. \quad (3)$$

Here the ϕ_i are pseudo-fermions situated on the lattice sites i and $\psi_i = Q_{ik}\phi_k$, where Q is the Clover–Wilson–Dirac matrix, which is specified by $C_{\rm SW}$ and the hopping parameter κ.

Knowing G_Q and G_q, the general form of a two-point correlation can be constructed from a heavy-quark propagating from site $(\mathbf{x}, t)$ to site $(\mathbf{x}', t+T)$ and a light-quark propagating from site $(\mathbf{x}', t+T)$ to site $(\mathbf{x}, t)$ as

$$\begin{aligned} C_2(T) &= \mathrm{Tr}\langle\Gamma^\dagger G_Q(\mathbf{x}, t; \mathbf{x}', t+T)\Gamma G_q(\mathbf{x}', t+T; \mathbf{x}, t)\rangle \\ &= 2\langle \mathrm{Re}\left[U^Q[\psi^*(\mathbf{x}, t+T)\phi(\mathbf{x}, t) \right. \\ &\quad \left. +\phi^*(\mathbf{x}, t+T)\psi(\mathbf{x}, t)]\right]\rangle. \end{aligned} \quad (4)$$

Here Γ is the spin structure of the heavy-quark light-quark vertices at t and $t+T$. In this case $\Gamma = \gamma_5$, since we are only interested in pseudoscalar mesons such as the B-meson. For clarity, the Dirac indices have been omitted.

Similarly, when the light-quark field is probed by an operator $\Theta(\mathbf{r})$ at $t = 0$ and the heavy-quark propagates from $t = -t_2$ to $t = t_1$

$$\begin{aligned} C_3(-t_2, t_1, \mathbf{r}) = \mathrm{Tr}\langle\Gamma^\dagger G_Q(\mathbf{x}, -t_2; \mathbf{x}, t_1)\Gamma\cdot \\ G_q(\mathbf{x}, t_1; \mathbf{x}+\mathbf{r}, 0)\Theta(\mathbf{r})G'_q(\mathbf{x}+\mathbf{r}, 0; \mathbf{x}, -t_2)\rangle. \end{aligned} \quad (5)$$

Here $\Theta = \gamma_4$ for the charge distribution and 1 for the matter (scalar) density.

The above has been written down for a single type of gauge field. However, the correlations can be greatly improved by fuzzing. In this case the basic links containing the gauge field have two fuzzings in addition to the original local field (L). In the standard notation of, for example [6], Fuzz1 has 2 iterations and Fuzz2 a further 6 iterations i.e. 8 in all. These will be referred to as F_1 and F_2. In both cases, the factor multiplying the basic link is $f_p = 2.5$ i.e.

$$\begin{aligned} &[\text{Projected fuzzed link}] = \\ &\quad f_p \cdot [\text{Straight link}] + [\text{Sum of 4 spatial U-bends}] \end{aligned}$$

with the quarks separated by a product of fuzzed links of length 1 lattice unit for Fuzz1 and 2 lattice units for Fuzz2, as discussed in [2]. With fuzzing included, C_2 and C_3 are now 3×3 matrices composed of matrix elements with the indices LL, LF_1, LF_2, $\mathrm{F}_1\mathrm{F}_1$, $\mathrm{F}_1\mathrm{F}_2$ and $\mathrm{F}_2\mathrm{F}_2$. This means that S-wave excited state energies and properties can now be studied in addition to those of the ground state.

3 Analysis

There are several ways of analysing the above correlation functions C_2 and C_3 in order to extract the quantities of interest i.e. energies and radial distributions. For a review of these methods see [7,8] – with more details using the present notation being found in [2]. We now draw upon experiences learnt in that reference.

Firstly, the two-point correlation data C_2 are analysed to give the energies (m_α) and eigenvectors ($\mathbf{v}$) for the states of the $Q\bar{q}$-system. These values of m_α and $\mathbf{v}$ are then fixed when analysing the three-point correlation data C_3 to give the charge and matter densities $x^{\alpha\beta}(r)$.

3.1 Analysis of the two-point correlation functions C_2

Consider the correlation function $C_2(T)$ as an $n\times n$ matrix – 3×3 in this case with the elements LL, LF_1, …, $\mathrm{F}_2\mathrm{F}_2$. Each element $C_{2,ij}(T)$ is then fitted with the form

$$C_{2,ij}(T) \approx \tilde{C}_{2,ij}(T) = \sum_{\alpha=1}^{M_2} v_i^\alpha \exp(-m_\alpha T) v_j^\alpha, \quad (6)$$

where M_2 is the number of eigenvalues and m_1 is the ground state energy of the heavy-light meson. The values of m_α and $v_{i,j}^\alpha$ are then determined by minimizing the difference between the C_2 data from the lattice and the form $\tilde{C}_2$. The function actually minimized is the usual

$$\chi^2 = \sum_{i,j}\sum_{T_{2,\min}}^{T_{2,\max}} \left[\frac{C_{2,ij}(T) - \tilde{C}_{2,ij}(T)}{\Delta C_{2,ij}(T)}\right]^2, \quad (7)$$

where $\Delta C_{2,ij}(T)$ is the statistical error on $C_{2,ij}(T)$ and $T_{2,\min}, T_{2,\max}$ are the minimum and maximum values of T_2 used in the fit.

The outcome is shown in Table 1, where we present 4 cases. In most of this paper we will concentrate on Case B, since this has both a good $\chi^2/n_{\rm dof}$ of 0.16 and sufficiently small errors on the state energies am_α. In contrast, Case A with $M_2 = 3$ has a large $\chi^2/n_{\rm dof}$ and Case C large errors on the am_α.

The table also shows – with Case Q – the earlier best fit in [2] to the 20 quenched configurations with $\beta = 5.7$. When comparing the am_α from the four cases, two points must be kept in mind:

1) Only differences of the am_α's have a meaning, since the lattice simulation generates different self-energies to the quarks in Case Q versus Cases A, B, C.
2) The table shows am_α, where the lattice spacing a is ≈ 0.17 fm for Case Q and ≈ 0.14 fm for Cases A, B, C.

Removing these two effects results in the $\Delta m_{\beta\alpha} = am_\beta - am_\alpha$ at the bottom of Table 1. There it is seen that, within the error bars, both Δm_{21} and Δm_{31} are unchanged in going from the 20 quenched configurations – after being scaled by the ratio of the lattice spacings 0.14/0.17 – to the preferred unquenched Case B. The best estimates are $\Delta m_{21} = 0.33(1)$, $\Delta m_{31} = 0.80(4)$ and $\Delta m_{41} = 1.05(6)$. This value of Δm_{21} is also the same as that obtained in [5], when the latter is also scaled by the lattice spacing ratio 0.14/0.17. However, it should be pointed out that in [5] the quenched approximation was used with the same parameters as in [2] but on a 12^3 spatial lattice.

Table 1. Values of the parameters am_α and v_i^α, needed for fitting the C_2-correlations. Case Q: 20 quenched configurations with $M_2 = 3$ and $T_{2,\min} = 4$ – referred to as Case 3 in [2]. Case A: 78 dynamical configurations with $M_2 = 3$ and $T_{2,\min} = 4$. Case B: 78 dynamical configurations with $M_2 = 4$ and $T_{2,\min} = 3$. Case C: 78 dynamical configurations with $M_2 = 4$ and $T_{2,\min} = 4$. The entries [...] for Δm_{21} and Δm_{31} include the ratio of lattice spacings 0.14/0.17. The entries marked with a dash are not applicable for $M_2 = 3$

am_α	Case Q	Case A	Case B	Case C
v_i^α	3×3 $T_{\min}=4$	3×3 $T_{\min}=4$	4×4 $T_{\min}=3$	4×4 $T_{\min}=4$
am_1	0.8721(19)	0.8580(11)	0.8340(40)	0.8280(88)
am_2	1.263(13)	1.2267(51)	1.166(11)	1.138(35)
am_3	1.94(30)	1.93(13)	1.632(42)	1.52(12)
am_4	–	–	1.889(58)	1.85(18)
v_{L}^1	0.4847(56)	0.4344(31)	0.3757(99)	0.359(24)
$v_{\mathrm{F}_1}^1$	1.519(10)	1.3779(70)	1.227(26)	1.181(65)
$v_{\mathrm{F}_2}^1$	0.8402(38)	0.8008(21)	0.731(12)	0.711(31)
v_{L}^2	0.816(16)	0.8405(65)	0.801(12)	0.757(55)
$v_{\mathrm{F}_1}^2$	0.644(49)	0.874(22)	1.185(44)	1.260(83)
$v_{\mathrm{F}_2}^2$	–0.251(33)	–0.115(12)	0.169(47)	0.26(12)
v_{L}^3	–0.28(22)	–0.348(97)	–0.459(29)	–0.534(85)
$v_{\mathrm{F}_1}^3$	2.2(1.4)	2.34(63)	1.36(16)	0.86(53)
$v_{\mathrm{F}_2}^3$	–1.13(81)	–0.84(39)	0.56(19)	0.61(25)
v_{L}^4	–	–	0.000(69)	0.05(19)
$v_{\mathrm{F}_1}^4$	–	–	–0.45(33)	–0.73(70)
$v_{\mathrm{F}_2}^4$	–	–	1.89(22)	1.64(78)
$n_{2,\mathrm{data}}$	54	48	54	48
$n_{2,\mathrm{param}}$	12	12	16	16
$n_{2,\mathrm{dof}}$	42	36	38	32
$\chi^2/n_{2,\mathrm{dof}}$	0.65	4.27	0.16	0.14
Δm_{21}	0.391(13) [0.322(11)]	0.369(5)	0.332(12)	0.310(36)
Δm_{31}	1.07(30) [0.88(24)]	1.07(13)	0.798(42)	0.69(12)
Δm_{41}	–	–	1.05(6)	1.02(18)

3.2 Analysis of the three-point correlation function for radial distributions

The analysis of the three-point correlation functions $C_3(\Theta, T, r)$ is performed using a generalisation of the one for C_2 in (6), namely,

$$C_{3,ij}(\Theta,T,r) \approx \tilde{C}_{3,ij}(\Theta,T,r) = \sum_{\alpha=1}^{M_3}\sum_{\beta=1}^{M_3} v_i^\alpha \mathrm{e}^{-m_\alpha t_1} x^{\alpha\beta}(r) \mathrm{e}^{-m_\beta (T-t_1)} v_j^\beta . \quad (8)$$

The m_α and $\mathbf{v}$-vectors are those obtained by minimizing the C_2 in (6) and, for each value of r, the $x^{\alpha\beta}(r)$ are varied to ensure a good fit to $C_{3,ij}(\Theta,T,r)$ by the model form $\tilde{C}_{3,ij}(\Theta,T,r)$.

Two forms of $x^{\alpha\beta}(r)$ are used here:

1) A non-separable (NS) form, where each $x^{\alpha\beta}(r)$ is treated as a single entity. Here we take $M_3 = M_2 = 4$. However, for the minimization algorithm migrad to converge to a reasonable solution, of the 10 possible values of $x^{\alpha\beta}(r)$ for a given value of r, only 7 are varied – the 4 $x^{\alpha\alpha}(r)$ and the 3 $x^{1\alpha}(r)$ with $\alpha \neq 1$. The other $x^{\alpha\beta}(r)$ are fixed to be zero.
2) A separable (S) form $x^{\alpha\beta}(r) = y_\alpha(r) y_\beta(r)$. Here, we take $M_3 = 3$ to give only three free parameters for each value of r – $y_1(r)$, $y_2(r)$ and $y_3(r)$.

In Table 2 results are given for both the NS and S forms of $x^{\alpha\beta}(r)$ and for different choices of $T_{2,\min}$, $T_{3,\min}$ – with the most representative solution being $S(3,8)$, the separable form with $T_{2,\min} = 3$ and $T_{3,\min} = 8$. The other choices give support to this solution and indicate the possible systematic error. In the penultimate column is given, in our opinion, the best overall estimate of the ground

Table 2. Estimates of the charge radial distributions $[x^{11}(r)]$ for the ground state. Separable case (S): $M_2 = 4$ in C_2, $M_3 = 3$ in C(3). $T_{2,\min} = 3$ and $T_{3,\min} = 6, 8$. Separable case (S): $M_2 = 4$ in C_2, $M_3 = 3$ in C(3). $T_{2,\min} = 4$ and $T_{3,\min} = 8$. Non-separable case (NS): $M_2 = M_3 = 4$ in C_2 and C_3 but $x^{ij} = 0$, when neither i nor j is 1. $T_{2,\min} = 3$ and $T_{3,\min} = 6, 8$. The column labelled Best Estimate is a summary of the previous 5 columns. The column labelled Approx. Estimate is from (10) for $M_2 = 3$ – Case A in Table 1. The line marked as 'ave' is the weighted mean $[6x^{11}(3,0,0) + 24x^{11}(2,2,1)]/30$

				S	S	S	NS	NS	Best	Approx.
	$T_{2,\min}$			3	3	4	3	3	Estimate	Estimate
	$T_{3,\min}$			6	8	8	6	8		
r	x	y	z							
0.00	0	0	0	0.0378(2)	0.0377(4)	0.0349(5)	0.0428(3)	0.0401(8)	0.038(4)	0.047(2)
1.00	1	0	0	0.01214(10)	0.0127(2)	0.0112(3)	0.01343(15)	0.0135(4)	0.0125(15)	0.015(1)
1.41	1	1	0	0.00704(8)	0.0075(2)	0.0068(2)	0.00831(10)	0.0091(3)	0.0080(15)	0.009(2)
1.73	1	1	1	0.00501(8)	0.0052(2)	0.0048(2)	0.00594(11)	0.0063(3)	0.0055(7)	0.0060(3)
2.00	2	0	0	0.00749(9)	0.0072(2)	0.0070(3)	0.00627(11)	0.0068(3)	0.0070(5)	0.0071(5)
2.24	2	1	0	0.00476(6)	0.00470(13)	0.0045(2)	0.00464(6)	0.0047(2)	0.0047(2)	0.0046(3)
2.83	2	2	0	0.00307(7)	0.0031(2)	0.0031(2)	0.00299(7)	0.0031(2)	0.0032(2)	0.0028(2)
3.00	3	0	0	0.00329(10)	0.0034(3)	0.0035(3)	0.00295(11)	0.0035(3)	0.0034(4)	0.0032(5)
3.00	2	2	1	0.00221(6)	0.00216(15)	0.0021(2)	0.00215(6)	0.0019(2)	0.00215(15)	0.0021(2)
3.00		ave		0.00243(6)	0.00241(13)	0.0023(2)	0.00231(5)	0.0022(2)	0.00240(14)	0.0023(2)
3.16	3	1	0	0.00234(6)	0.00244(14)	0.0025(2)	0.00226(6)	0.0026(2)	0.0025(3)	0.0024(2)
3.61	3	2	0	0.00164(6)	0.00178(13)	0.0019(2)	0.00166(5)	0.00188(14)	0.0018(2)	0.0017(2)
4.00	4	0	0	0.00141(10)	0.0015(3)	0.0016(4)	0.00126(10)	0.0014(3)	0.0015(3)	0.0012(2)
4.12	4	1	0	0.00095(5)	0.00105(13)	0.0011(2)	0.00092(5)	0.00115(15)	0.0011(2)	0.0009(1)
4.24	3	3	0	0.00082(8)	0.0010(2)	0.0010(3)	0.00085(7)	0.0011(2)	0.0010(3)	0.0008(2)
4.47	4	2	0	0.00074(5)	0.00075(12)	0.0007(2)	0.00076(5)	0.00068(15)	0.00070(15)	0.0005(2)
5.00	4	3	0	0.00067(6)	0.00080(10)	0.0009(2)	0.00078(5)	0.00115(14)	0.0009(3)	0.0008(2)
5.10	5	1	0	0.00046(6)	0.00053(14)	0.0006(2)	0.00050(5)	0.0007(2)	0.0006(2)	0.0005(2)
5.39	5	2	0	0.00033(8)	0.00044(14)	0.0005(2)	0.00036(5)	0.0006(2)	0.0005(2)	0.0003(1)
5.83	5	3	0	0.00020(5)	0.00026(12)	0.0003(2)	0.00027(5)	0.0005(2)	0.00035(15)	0.0004(2)

state charge density with error. The last column shows estimates using Case A in Table 1. As shown in [2], in this case the v_i^α matrix is square and so can be inverted to give the matrix u_i^α. Estimates $\bar{C}_{3,\alpha\beta}(T)$ can then be written down directly as

$$\bar{C}_{3,\alpha\beta}(T) = u_i^\alpha C_{3,ij}(T) u_j^\beta. \tag{9}$$

In this case

$$x^{11}(r) = \lim_{T\to\infty} \frac{\langle \bar{C}_{3,11}(T,r)\rangle}{\langle \bar{C}_{2,11}(T)\rangle}. \tag{10}$$

Unfortunately, the extraction of the asymptotic $T \to \infty$ limit is somewhat subjective and gives the estimates in the last column in Table 2. In all the cases listed, within errors these agree with the previous column. However, this approach did show that the data from some of the larger values of (x, y) were not good and so these are dropped in the subsequent discussion. Also, for reasons to be discussed in Sect. 4.5, neither the (2,2,1) data nor the weighted average of (3,0,0)/(2,2,1) are included in the following analysis.

In Table 3 similar estimates are given for charge densities involving excited states. Also this table contains a summary of the $x^{11}(r)$ and $x^{12}(r)$ matter radial distributions, which were extracted using both the NS and S forms for different choices of $T_{2,\min}$, $T_{3,\min}$ – just as in the charge case. However, these signals are somewhat weaker than for the charge, so that no meaningful matter distributions could be extracted for $r \geq 4a$.

In Fig. 3 the best estimates of the charge and matter distributions from Tables 2 and 3 are compared. To guide the eye we also show lines depicting the lattice exponential fits to be discussed later in Sect. 4.1. Here it is clearly seen that the range of the charge distribution is longer than that of the matter distribution. Furthermore, this figure also contains the charge and matter densities obtained with the quenched approximation in [2]. For this comparison, the results of [2] are scaled from lattice spacing $a_{0.14}$ to $a_{0.17}$ by simply $r_{0.17} \to \rho r_{0.17}$ and $x^{11}(r_{0.17}) \to \rho^{-3} x^{11}(r_{0.17})$, where $\rho = 0.17/0.14$. Here it is seen that the present results using dynamical fermions are indistinguishable from those using the quenched approximation. It will be seen later in the last two columns of Table 4, that this near equality is also reflected in the charge sum rules with both giving $x^{11} = 1.4(1)$. As discussed in [9] and [10], this is of particular interest in the matter case,

Table 3. Best estimates of radial distributions of charge and matter distributions involving also excited states. The column labelled x^{11} (AE) is an approximate estimate from (10) for $M_2 = 3$ – Case A in Table 1. The entry '–' implies that a reasonable signal could not be obtained and the entry 'ave' has the same definition as in Table 2

	Charge			Matter		
r	x^{12}	x^{13}	x^{22}	x^{11}	x^{11} (AE)	x^{12}
0.00	0.079(4)	−0.050(2)	0.18(2)	0.045(3)	0.058(2)	0.090(5)
1.00	0.0160(5)	0.015(2)	0.021(3)	0.0133(5)	0.016(1)	0.009(1)
1.41	0.0045(15)	0.010(2)	0.003(1)	0.0073(7)	0.0076(6)	−0.001(1)
1.73	0.0010(10)	0.007(2)	0.005(4)	0.0049(5)	0.0045(6)	−0.0030(7)
2.00	0.0020(5)	0.0005(15)	0.0005(4)	0.006(1)	0.0054(5)	−0.003(1)
2.24	0.0000(3)	0.0022(5)	0.0000(1)	0.0038(4)	0.0032(3)	−0.0030(7)
2.83	−0.0010(3)	−0.0005(10)	0.0003(2)	0.0017(2)	0.0013(3)	−0.0015(3)
3.00	−0.0009(4)	−0.0018(15)	0.0003(2)	0.0014(3)	0.0013(3)	−0.0010(3)
3.00	−0.0007(2)	0.0010(10)	0.0003(2)	0.0016(2)	0.0009(2)	−0.0018(5)
ave	−0.0007(2)	0.0004(9)	0.0003(2)	0.0016(2)	0.0010(2)	−0.0016(4)
3.16	−0.0009(2)	−0.0010(10)	0.0003(2)	0.0009(2)	0.0009(3)	−0.0005(5)
3.61	−0.0010(2)	−0.0010(5)	0.0006(2)	0.0007(2)	0.0005(3)	−0.0008(4)
4.00	−0.0007(2)	−0.0018(12)	0.0005(3)	–	–	–
4.12	−0.00045(15)	−0.0010(8)	0.0003(2)	–	–	–
4.24	−0.00050(15)	−0.0011(8)	0.0005(3)	–	–	–
4.47	−0.00040(15)	−0.0000(5)	0.00025(15)	–	–	–
5.00	−0.0007(2)	−0.0010(5)	0.00065(15)	–	–	–
5.10	−0.00040(15)	−0.0008(4)	0.0004(2)	–	–	–
5.39	−0.0003(2)	−0.0005(3)	0.0003(2)	–	–	–
5.83	−0.0003(2)	0.0001(3)	0.0001(2)	–	–	–

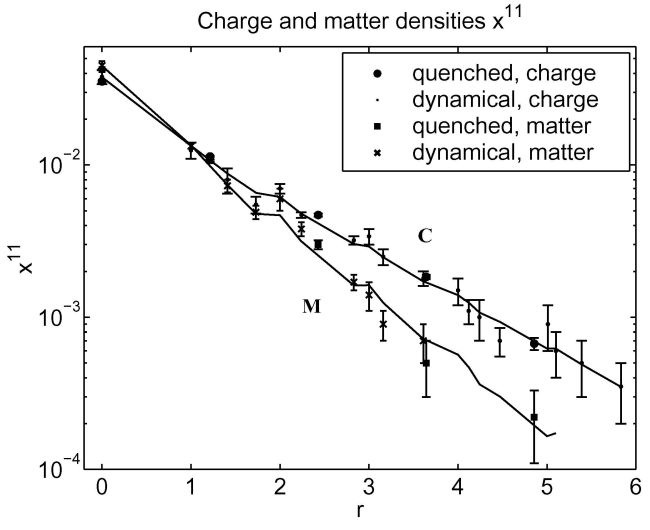

Fig. 3. The ground state charge (C) and matter (M) densities $[x^{11}(r)]$ as a function of r in units of a. The lines shows a fit to these densities with a sum of two lattice exponential functions. The scaled quenched results of [2] are also shown by filled circles and squares

since there disconnected contributions could arise that are dependent on the quenched versus unquenched. Any difference would then be due to the effect of the quark condensate. Clearly, with the present data no such effect can be detected. However, it must be remembered that here the sea quarks have the same mass as the valence quarks i.e. about that of the strange quark. It is possible that using sea quarks with more realistic u, d quark masses the above conclusion would be different. This observation that full QCD and the quenched approximation do not differ significantly has been seen many times before.

In Fig. 4a, for the charge density ratio x^{12}/x^{11}, only the errors for the separable analysis with $T_{2,\min} = 3$ and $T_{3,\min} = 8$ are shown, since the other analyses have similar errors. There a distinct node is seen at about 2.2 lattice spacings i.e. at ≈ 0.3 fm. Such a node is natural for x^{12}, since it involves the excited S-wave state. On the other hand, for the matter density – as seen in Fig. 4c – the node is near to $1.5a \approx 0.2$ fm. Figure 4b shows the various analyses for the charge density ratio x^{13}/x^{11}. Here the node structure is less clear. One node is seen at about 2.8 lattice spacings i.e. at ≈ 0.4 fm. But a second possible node at about 0.6 lattice spacings, i.e. at ≈ 0.1 fm, depends on the one value of x^{13} at $r = 0$. However, we have no reason to suspect that this is purely a lattice artefact. Furthermore, for second excited S-wave states a second node is not unexpected. Similar comments hold for the matter density ratio x^{13}/x^{11} in Fig. 4d. The node structure of x^{22} – the charge density of the first excited state – is not at all clear. If x^{22} is expressed in the separable form $y_2(r)y_2(r)$, then the zero that should appear at about $2a$ is not seen very distinctly in comparison with that seen in Figs. 4a or c for x^{12}/x^{11}.

The above figures show directly the various charge densities $x^{\alpha\beta}(r)$. However, it is also of interest to see the struc-

Table 4. The charge and matter sum rules in the ground state x^{11} and between excited states. The symbols N and NS are as in Table 2. Q refers to the quenched results (case 3) in [2]. The entries marked with a dash are not applicable for $M_3 = 3$

$T_{2,\min}/T_{3,\min}$ $x^{\alpha\beta}$	S (3/6)	S (3/8)	S (4/8)	NS (3/6)	NS (3/7)	NS (3/8)	Q-NS (3/8)
Charge							
x^{11}	1.12(3)	1.26(6)	1.26(8)	1.29(4)	1.36(6)	1.42(11)	1.41(5)
x^{12}	0.09(3)	−0.10(9)	−0.05(12)	−0.28(7)	−0.40(12)	−0.5(2)	−0.5(2)
x^{13}	0.02(9)	−0.3(4)	−0.1(4)	0.09(11)	−0.2(2)	−0.3(6)	0(1)
x^{14}	–	–	–	−0.1(2)	−0.4(4)	−0.5(1.1)	–
x^{22}	0.008(5)	0.007(14)	0.002(9)	0.8(2)	0.9(3)	1.1(6)	0.9(9)
$\chi^2/n_{\rm dof}$	2.52	0.65	0.63	0.31	0.13	0.09	0.26
Matter							
x^{11}	0.66(5)	0.85(14)	1.0(2)	0.73(8)	0.83(11)	1.1(2)	0.38(15)
x^{12}	−0.15(6)	−0.5(2)	−0.6(3)	−0.27(13)	−0.4(2)	−0.8(4)	−0.1(5)
x^{13}	−0.4(2)	−1.7(1.0)	−1.6(9)	−0.3(2)	−0.9(4)	−2.7(1.2)	−1(5)
x^{14}	–	–	–	−0.2(3)	−0.8(7)	−3.2(2.2)	–
x^{22}	0.04(3)	0.3(2)	0.4(4)	0.2(3)	0.2(6)	0.2(1.2)	1(2)
$\chi^2/n_{\rm dof}$	0.46	0.29	0.25	0.31	0.25	0.12	0.35

ture of the individual terms $y_\alpha(r)$ in the separable form $x^{\alpha\beta}(r) = y_\alpha(r)y_\beta(r)$. These are shown in Fig. 5 for both the charge and the matter. Figure 5a shows clearly that $y_1(r)$ for the charge has a significantly longer range than for the matter. Also as seen in Fig. 5b both of the $y_2(r)$ exhibit a distinct node and are responsible for the nodes in the separable form of the density x^{12} already seen in Fig. 4a. We do not plot $y_3(r)$, since the signal/error ratio is too small.

As discussed at the end of the Introduction, the $y_\alpha(r)$ can possibly be interpreted as wave functions for the state α. However, there are other radial distributions associated with the $Q\bar{q}$ system that can also be interpreted as wave functions. These are the Bethe-Salpeter wavefunctions $[w_\alpha(r)]$ discussed in [5]. They were extracted by assuming the hadronic operators $C_{2,\alpha\alpha}(r_1, r_2, T)$ to be of the form $w_\alpha(r_1)w_\alpha(r_2)\exp(-m_\alpha T)$, where the sink and source operators are of spatial size r_1 and r_2. In Fig. 5 a comparison is made between the above values of $y_1(r)$ and $y_2(r)$ and the corresponding results form [5] for $w_1(r)$ and $w_2(r)$, where the latter have been normalised so that $w_1(0) = y_1(0)$ and $w_2(0) = y_2(0)$ and the values of r scaled. Even though they do bear some similarities, it should be added that there are several reasons why these two types of wave function should *not* agree in detail with each other. In particular, the $[w_\alpha(r)]^2$ cannot be identified as a charge or matter distribution.

3.3 Charge sum rule

In addition to measuring $C_3(r)$ for various values of r, the correlation where r is summed over the whole lattice is also obtained. This leads to the charge sum rule as discussed in [2]. The actual values of this sum rule are extracted using (8), where the $x^{\alpha\beta}$ are now independent of r. The outcome – as shown in Table 4 – is that x^{11} is $\approx 1.3(1)$ consistent with the earlier quenched result. The fact that x^{11} is not unity – as expected in the continuum limit – can be qualitatively understood by introducing a renormalisation factor of $\approx 1/1.3 \approx 0.8$ into the basic γ_4 vertex used to measure the charge density. Such a factor of this magnitude is reasonable as shown in [11].

It is also reassuring that the $x^{\alpha\beta}$ with $\alpha \neq \beta$ are, in general, consistent with zero – as expected in the continuum limit. However, the interpretation of x^{22} is less clear. The non-separable (NS) case gives $x^{22} \approx 1.0(4)$ – again a reasonable value in the continuum limit – whereas the separable case (S) yields $x^{22} \approx 0.0$. This suggests that the separable approximation may be less appropriate for excited states.

In Table 4 we also show the matter sum rule. These have a somewhat wider spread of values with 0.9(1) being a reasonable compromise – a number that is about twice the estimate of 0.38(15) for the quenched calculation of [2]. Perhaps this is an indication – unlike the matter radial distributions in Fig. 3 – that the quenched and unquenched results can differ even with the present sea quark masses of about the strange quark. However, we do not have the data to cross check with [9] and [10], which advocate the existence of such a difference for the matter sum rule.

4 Form of radial dependence

The results in Table 2 are presented as simply a series of numbers for each value of r or (x, y, z). However, it would be more convenient and perhaps illuminating, if they could be parametrized in some simple way. This can

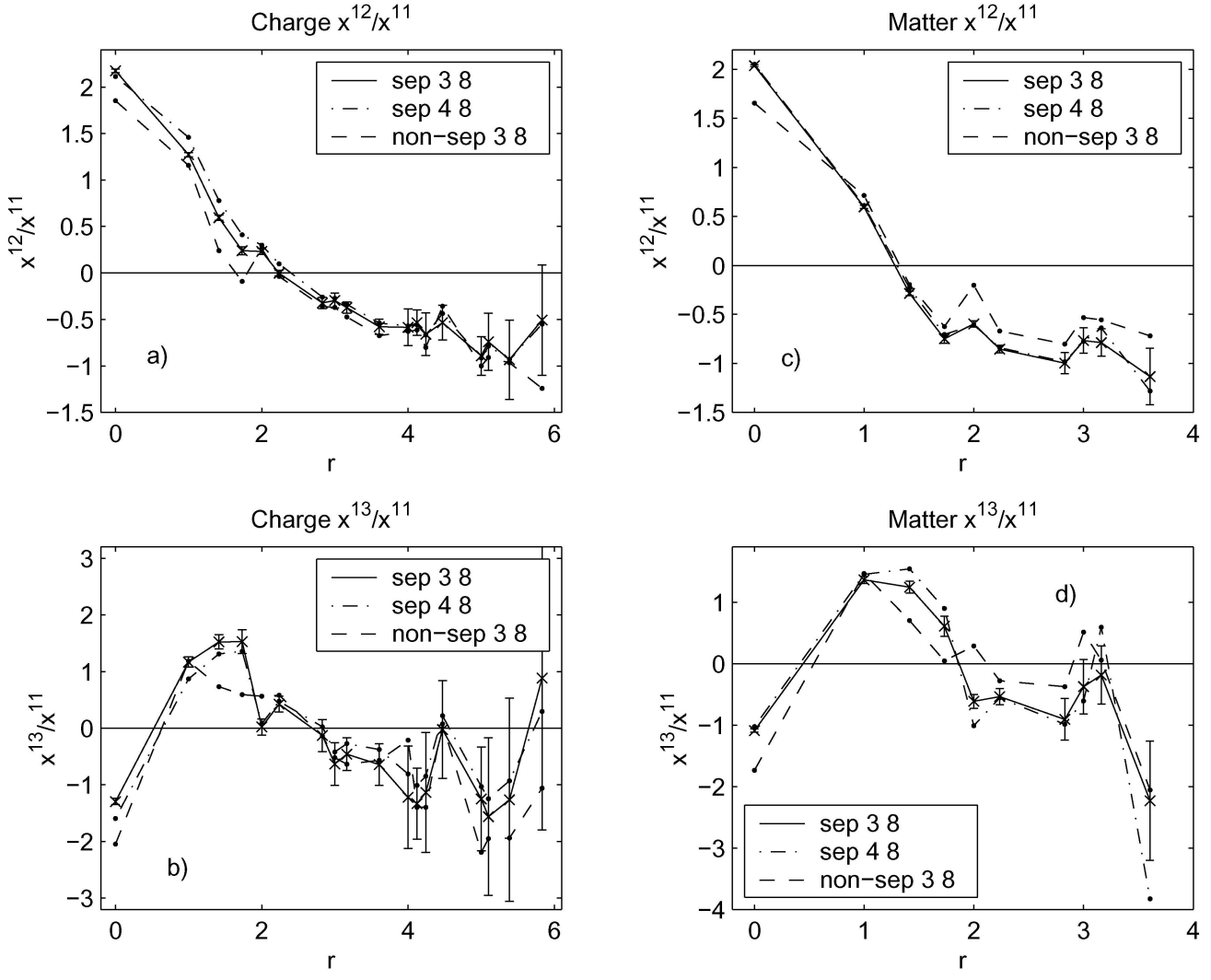

Fig. 4. **a** and **b**: the ratios x^{12}/x^{11} and x^{13}/x^{11} for the charge distribution. **c** and **d**: these ratios for the matter distribution

be done either in coordinate or momentum space – the topics of the next subsections.

4.1 Coordinate space fit

Here we assume that the radial dependences of the lattice data in Table 2 can be represented in terms of exponential (E), Yukawa (Y) or gaussian (G) functions. Then the strategy is to first fit the data at the largest values of r with a single form in order to parametrize the longest ranged part of the data, where it is expected that lattice artefacts will be less. This range is then used as a starting point, when the data at all values of r are fitted by adding a second form.

The reason for using exponential and Yukawa radial functions is that they arise naturally as propagators in quantum field theory – usually in their momentum space form $(q^2+m^2)^{-1}$. However, if we go away from quantum field theory and attempt to understand the radial dependences in terms of wavefunctions from, for example, the Dirac equation, then gaussian forms can then arise.

4.1.1 Lattice exponential, Yukawa and gaussian fits to the charge and matter densities

As seen in Fig. 3, the data is far from being a smooth function of r – indicating lattice artefact effects. Therefore, lattice versions of the exponential, Yukawa and gaussian forms (LE, LY, LG) are used. In [12] the lattice form of the Coulomb function $(1/r)$ is written as

$$\left[\frac{1}{\mathbf{r}}\right]_{\mathrm{LC}} = \frac{\pi}{aL^3}\sum_{\mathbf{q}}\frac{\cos(\mathbf{r}.\mathbf{q})}{D}. \qquad (11)$$

Here L is the lattice size along one axis and

$$D = \sum_{i=1}^{3}\sin^2(aq_i/2), \text{where}$$
$$aq_i = 0, \frac{2\pi}{L}, \ldots, \frac{2\pi(L-1)}{L}, \mathbf{q} \neq 0.$$

In this subsection, for clarity, the lattice spacing a is shown explicitly. For the above Yukawa form, (11) is easily gen-

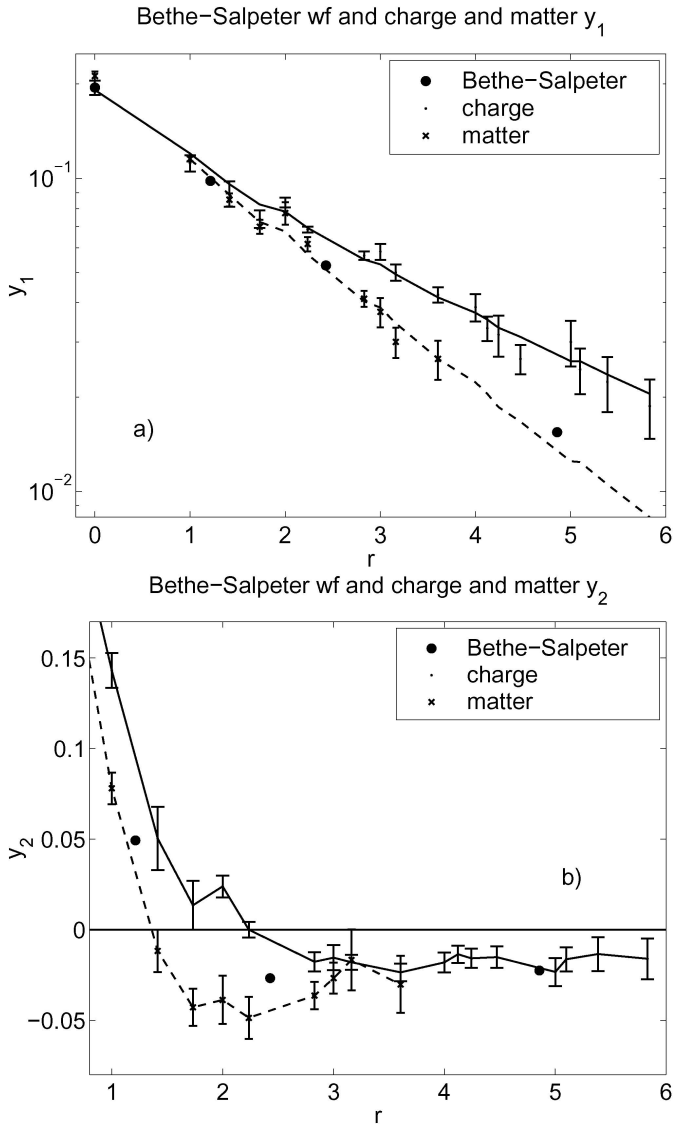

Fig. 5a,b. The separable "wavefunctions" y_1 and y_2 defined in the density $x^{\alpha\beta}(r) = y_\alpha(r)y_\beta(r)$. **a** y_1 – Solid line for the charge, dashed for the matter, solid circles the Bethe-Salpeter wavefunction from [5], **b** y_2 – notation as in **a**

eralised to

$$\left[\frac{\exp(-\mathbf{r}/r^{\rm LY})}{\mathbf{r}}\right]_{\rm LY} = \frac{\pi}{aL^3}\sum_{\mathbf{q}}\frac{\cos(\mathbf{r}.\mathbf{q})}{D+0.25[a/r^{\rm LY}]^2}. \quad (12)$$

However, now the point $\mathbf{q}=0$ can be included in the sum, since it is no longer a singularity – provided $1/r^{\rm LY} \neq 0$. Similarly, lattice forms of the exponential and gaussian can be obtained by simply replacing in the usual Fourier transform the q^2 factors by their lattice equivalent $\frac{4}{a^2}\sum_{i=1}^{3}\sin^2(aq_i/2) = \frac{4D}{a^2}$. This results in

$$\left[\mathrm{e}^{-\mathbf{r}/r^{\rm LE}}\right]_{\rm LE} = \frac{\pi a}{2r^{\rm LE}L^3}\sum_{\mathbf{q}}\frac{\cos(\mathbf{r}.\mathbf{q})}{\left[D+0.25(a/r^{\rm LE})^2\right]^2}, \quad (13)$$

$$\left[\mathrm{e}^{-(\mathbf{r}/r^{\rm LG})^2}\right]_{\rm LG} = \left[\frac{r^{\rm LG}\sqrt{\pi}}{aL}\right]^3\sum_{\mathbf{q}}\cos(\mathbf{r}.\mathbf{q})\mathrm{e}^{-D(r^{\rm LG}/a)^2}. \quad (14)$$

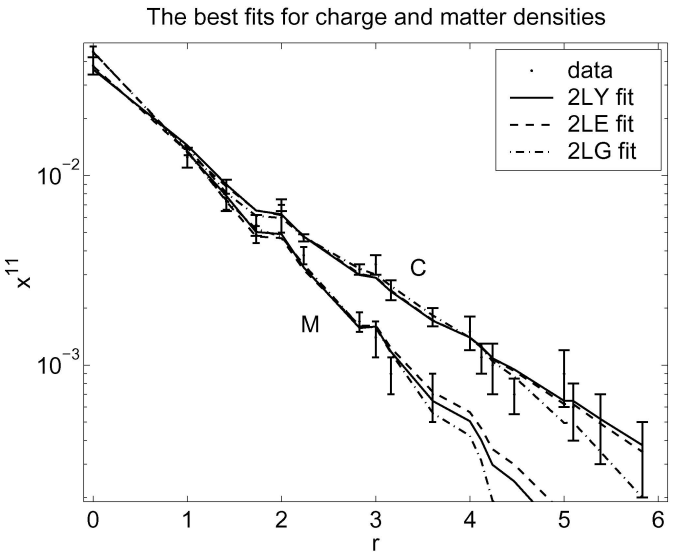

Fig. 6. Fit to the lattice data in Table 2 with lattice exponential (2LE), Yukawa (2LY) and gaussian (2LG) forms in Table 5

Using these lattice forms yields columns 2LY, 2LE and 2LG in Tables 5 and 6 for the charge and matter respectively. For comparison the parameters for the corresponding non-lattice forms are given in columns 2Y, 2E and 2G. Here the prefix '2' indicates that each form contains two terms – as needed by the strategy outlined above. It is seen that the values of $r_0^{\rm F}$ for all three lattice forms 2LE, 2LY and 2LG are quite similar to their 2E, 2Y and 2G counterparts. The outcome is that the lattice forms are able to reproduce some of the structure especially near $r = 2$ and 3 – as seen in Figs. 3 and 6. This is also reflected in the $\chi^2/n_{\rm dof}$'s being now less than unity for the charge case and < 1.2 for the matter. At first sight the two parametrizations 2LE and 2LY look very different, since (12) and (13) have such dissimilar forms. In addition, in 2LE the two terms add up, whereas in 2LY they cancel, since $a_0^{\rm 2LY}$ and $a_1^{\rm 2LY}$ have opposite signs in order to dampen the $1/r$ effect at small r. However, later we shall see that, in practice, 2LE and 2LY behave in very similar ways – with little numerical preference for one over the other.

The conclusion from this subsection is that all three parametrizations 2LE, 2LY and 2LG are acceptable, since each can fit all the lattice data with $\chi^2/n_{\rm dof}$'s comparable to unity.

4.1.2 Lattice exponential, Yukawa and gaussian fits to the separable form of the charge and matter densities

The above has concentrated on fitting directly the ground state charge density $x^{11}(r)$ in (8). However, in Sect. 3.2 a second and possibly more natural parametrization – a separable form $x^{\alpha\beta}(r) = y_\alpha(r)y_\beta(r)$ – was introduced. This resulted in the data shown in columns S of Table 2. Here we consider that the $y_1(r)$ are simply $\sqrt{x^{11}(r)}$, where the latter are the Best Estimate values in Table 2. The corresponding fits 2LES, 2LYS and 2LGS, with the above forms

Table 5. Fits to the charge lattice data with exponential, Yukawa and Gaussian forms. Column 2E refer to the exponential form $\sum_{0,1} a_i^{\rm E} \exp(-r/r_i^{\rm E})$. Column 2Y refer to the Yukawa form $\sum_{0,1} a_i^{\rm Y} \exp(-r/r_i^{\rm Y})/r$. Column 2G refer to the gaussian form $\sum_{0,1} a_i^{\rm G} \exp(-(r/r_0^{\rm G})^2)$. Also fits to the lattice data with the lattice Yukawa (2LY), exponential (2LE) Gaussian (2LG) forms from (12), (13) and (14). $I_{\rm E} = 8\pi \sum_{0,1} a_i^{\rm E}(r_i^{\rm E})^3$, $I_{\rm Y} = 4\pi \sum_{0,1} a_i^{\rm Y}(r_i^{\rm Y})^2$, $I_{\rm G} = \pi^{3/2} \sum_{0,1} a_i^{\rm G}(r_i^{\rm G})^3$ are the spacial integrals of these functions. The entries marked as * are fixed in the minimization

Form(F)	2E	2LE	2Y	2LY	2G	2LG
$a_0^{\rm F}$	0.0250(22)	0.0245(21)	0.069(10)	0.066(3)	0.0086(5)	0.0075(7)
$r_0^{\rm F}$	1.36(6)	1.37(6)	1.70(6)	1.78(7)	2.92(9)	3.07(12)
$a_1^{\rm F}$	0.013(5)	0.373*	–0.073*	–0.060*	0.0293(41)	0.019(4)
$r_1^{\rm F}$	0.2(4)	0.116(15)	1.00(17)	1.12(11)	0.75(7)	0.99(15)
$I^{\rm F}$	1.6(3)	1.6(3)	1.6(5)	1.7(3)	1.3(1)	1.3(2)
$\chi^2/n_{\rm dof}$	1.32	0.81	1.33	0.94	1.47	0.93

Table 6. Fits to the matter lattice data with exponential, Yukawa and Gaussian forms. In 2LY† the $r = 0$ data point is not fitted. Other notation as in Table 5

Form (F)	2E	2LE	2Y	2LY†	2G	2LG
$a_0^{\rm F}$	0.036(20)	0.0345(26)	0.178(12)	0.186(23)	0.0105(12)	0.0101(16)
$r_0^{\rm F}$	0.91(13)	0.938(39)	1.04(12)	0.92(6)	2.11(9)	2.14(11)
$a_1^{\rm F}$	0.009(20)	0.561*	–0.168*	–0.207*	0.0346(32)	0.034(10)
$r_1^{\rm F}$	0.45(55)	0.099(11)	0.90(18)	0.71(12)	0.71(4)	0.70(12)
$I^{\rm F}$	0.7(5)	0.73(10)	0.7(9)	0.7(6)	0.62(10)	0.62(13)
$\chi^2/n_{\rm dof}$	1.80	1.16	1.74	1.11	1.11	1.00

Table 7. Fits to the separable function $y_1(r)$ defined as $y_1(r) = (x^{11})^{1/2}$, where the x^{11} are the charge density values labelled as Best Estimate in 2. Notation as in Table 5

Form (LFS)	2ES	2LES	2YS	2LYS	2GS	2LGS
$a_0^{\rm LFS}$	0.159(7)	0.156(8)	0.47(3)	2.4310(60)	0.092(3)	0.083(4)
$r_0^{\rm LFS}$	2.73(12)	2.59(9)	4.40(21)	2.86(11)	4.19(12)	4.44(17)
$a_1^{\rm LFS}$	0.036(13)	0.0422*	–0.49*	–2.4196*	0.102(11)	0.065(6)
$r_1^{\rm LFS}$	0.2(5)	0.41(17)	1.66(22)	2.43(10)	0.85(9)	1.24(15)
$\chi^2/n_{\rm dof}$	1.32	1.11	1.33	1.11	1.75	1.07

are shown in Tables 7 and 8. For comparison the results from using the usual non-lattice forms 2ES, 2YS and 2GS are also included.

The conclusion to be drawn from this section is that the lattice data extracted in Sect. 3 can be well fitted by any of the three lattice forms in (12), (13) or (14) – numerically none of them is superior and also none can be rejected. This statement applies not only to the direct parametrizations of the density as in Sect. 4.1.1 but also to the separable form in Sect. 4.1.2.

4.2 Momentum space fit

Often it is more convenient to view data in momentum space by making the transformation

$$x^{\alpha\beta}(\mathbf{k}) = \sum_{\mathbf{r}} \cos(\mathbf{k}.\mathbf{r}) x^{\alpha\beta}(\mathbf{r}), \tag{15}$$

where the $\mathbf{r}$ summation should be over the whole 3-dimensional L^3 lattice. This would mean, in the present calculation, summing x, y and z over the ranges -7 to $+8$. If the lattice Yukawa, exponential and gaussian expressions in (12), (13) and (14), written as

$$x(\mathbf{r}) = \frac{\pi}{L^3} \sum_{\mathbf{q}} \cos(\mathbf{r}.\mathbf{q}) F(\mathbf{q}), \tag{16}$$

are now used to parametrize $x(\mathbf{r})$, then we simply get

$$x(\mathbf{k}) = \pi F(\mathbf{k}). \tag{17}$$

Here use has been made of the identity $\sum_{\mathbf{r}} \cos[\mathbf{r}.(\mathbf{k}-\mathbf{q})] = L^3 \delta_{\mathbf{k},\mathbf{q}}$. From (15) we see that the sum rule discussed earlier is now directly $x(\mathbf{k}=0) = \pi F(0) = I^{\rm F}$, where the $I^{\rm F}$

Table 8. Fits to the separable function $y_1(r)$ defined as $y_1(r) = (x^{11})^{1/2}$, where the x^{11} are the matter density values in Table 3. In 2LY† the $r = 0$ data point is not fitted. Other notation as in Table 5

Form (LFS)	2YS	2LYS†
$a_0^{\rm LFS}$	0.75(4)	0.74(4)
$r_0^{\rm LFS}$	2.39(27)	2.25(18)
$a_1^{\rm LFS}$	–0.728*	–0.774*
$r_1^{\rm LFS}$	1.52(28)	1.36(20)
$\chi^2/n_{\rm dof}$	1.84	1.25

are defined in the caption of Table 5. The other fourier components with $\mathbf{k} \neq 0$ are simply $\pi F(\mathbf{k})$.

4.2.1 The inclusion of lattice data directly into (15)

The result in (17) is not surprising, since it is simply the Fourier transform of a Fourier transform. However, if – where available – the lattice data of Table 2 are used for the $x^{\alpha\beta}(\mathbf{r})$ in (15) and the form in (16) only used for the missing densities, then the result should be an improved estimate of the $x^{\alpha\beta}(\mathbf{k})$. A measure of this can be obtained by fitting this improved estimate with the forms $F(\mathbf{k}, a_i, r_i)$ in (12), (13) and (14), but where the parameters a_i, r_i are tuned using the Minuit minimization package and are not the ones appearing in Tables 5 and 7.

As we shall see in the next subsection, the fits of main interest are 2LY, 2LE and 2LYS, since they possibly have a physical interpretation. However, this fitting procedure presents some problems, since we are attempting to fit 165 numbers with only four parameters $(a_{i=0,1}, r_{i=0,1})$ – the $x^{\alpha\beta}(\mathbf{k})$ with $k_i = 0, \frac{2\pi}{L}, \ldots, \frac{2\pi(L-1)}{L}$. Another problem is the choice of function to be minimized. We consider two options:

(i) $N_1 = \left[x_{\rm FT}(\mathbf{k}) - x_{\rm model}(\mathbf{k})\right]^2$ and
(ii) $N_2 = \left[x_{\rm FT}(\mathbf{k})/x_{\rm model}(\mathbf{k}) - 1\right]^2$,

where the $x_{\rm FT}(\mathbf{k})$ are the Fourier transforms (with or without direct data inclusion) defined in (15) and the $x_{\rm model}(\mathbf{k})$ are the $\pi F(\mathbf{k})$ in (16). Since the $x_{\rm FT}(\mathbf{k})$ decrease rapidly as $\mathbf{k}$ increases, Option (i) emphasizes the smaller values of $\mathbf{k}$ and is appropriate for extracting r_0, which is the longer range. In principle, Option (ii) is better since it should give an overall fit to the $x_{\rm FT}(\mathbf{k})$. But in practice, it tends to be unstable yielding either unacceptable solutions or very large error bars.

If the 2LY fit to the charge density in Table 5 is analysed with a Yukawa form, then Options (i) and (ii) give poles at $r_0 = 1.78(24)$ and 1.78(9) respectively – see Table 9. This is to be compared with the input value of 1.78(7) in Table 5. A similar strategy can be applied to the improved $x^{11}(\mathbf{k})$ generated from (15), where $x^{11}(\mathbf{r})$ now contains directly lattice data wherever possible. In this case, Options (i) and (ii) yield $r_0 = 1.78(20)$ and 3.3(1.0) i.e. the result from Option (i) is not distinguishable from using the fitted expression in (12) for all values of r, whereas that from Option (ii) is unstable. Similarly, if the 2LE fit in Table 5 is analysed with an exponential form, then Options (i) and (ii) give poles at $r_0 = 1.38(22)$ and 1.38(15) respectively. This is to be compared with the input value of 1.37(6) in Table 5. For the improved form of the density the two Options yield 1.39(23) and 1.41(16). Again Option (i) is indistinguishable from using only the fit values of $x^{11}(\mathbf{r})$. However, now option (ii) is more stable than before.

Table 9. The value of r_0 from fits to the Fourier transform of the charge density $x^{11}(\mathbf{r})$ as defined in (15). Row A: r_0 directly from Tables 5 and 7. Row B: r_0 extracted from the Fourier Transform of $x^{11}(\mathbf{r})$ when these are expressed in terms of the analytic expressions in (12), (13) and (14) with the parameters in Tables 5 and 7. Option (i) is used for defining the χ^2. Row C: Same as Row A but using Option (ii). Row D: The $x^{11}(\mathbf{r})$ are the same as in row B and C, except that the data from Table 2 is used wherever possible – Option (i) used. Row E: Same as Row D but using Option (ii)

Extract with	2LY	2LE
A	1.78(7)	1.37(6)
Form	2LY	2LE
B	1.78(24)	1.38(22)
C	1.78(9)	1.38(15)
D	1.78(20)	1.39(23)
E	3.3(1.0)	1.41(16)

The conclusion to be drawn from Table 9 is that the parametrizations in Tables 5 and 7 are so good that any improvements on r_0 due to the inclusion of explicit lattice data cannot be detected. Therefore, in the following discussions the Fourier transforms based purely on Tables 5 and 7 will, in general, be used.

4.3 Possible interpretations of the above fits

In the above, the use of the various forms E, Y, ..., LYS, LGS is considered as a purely numerical exercise. However, one can also ask about any theoretical interpretation of, or preference for, one form over the others. As we shall see below, in some cases, this is best discussed in momentum space. Also, since the inclusion of the original data has little effect, the fourier transform of the charge density should be well described by simply $\pi F(\mathbf{k})$. Therefore, the discussion below focusses on the interpretation of the different forms of $\pi F(\mathbf{k})$. Here several possibilities are suggested:

4.3.1 Y and LY

These forms can be directly identified as the propagators of a single particle. In the Y form – $a_i^{\rm Y} \exp[-r/r_i^{\rm Y}]/r$ – the masses of the propagating particles are simply $1/r_i^{\rm Y}$. Also for LY by writing the denominator of (12) in the continuum limit as $\frac{q^2}{4} + 0.25[a/r_i^{\rm LY}]^2$, we see that these masses

can also be identified as $1/r_i^{\rm LY}$. For the charge case these will be vector particles, whereas for the matter case they are scalars. From the fits to the charge distributions in Table 5, the vector masses that emerge are – in lattice units of about 1.4 GeV – $am^v_{0,2\rm LY} = 0.56 \pm 0.02$ and $am^v_{1,2\rm LY} = 0.89 \pm 0.11$ with the corresponding scalar masses from the matter distribution in Table 6 being $am^s_{0,2\rm LY} = 1.09 \pm 0.06$ and $am^s_{1,2\rm LY} = 1.4 \pm 0.2$.

4.3.2 E and LE

Looking at Fig. 2 for the three-point correlations, a cut in the T-direction intersects the two light-quark propagators $G_q(t_1 \to 0)$ and $G_q(0 \to -t_2)$. In comparison, the lattice exponential form in (13) also contains a product of two propagator-like terms $1/[D + 0.25(a/r^{\rm E})^2]$. This then suggests that the exponential form may be interpreted as the *product of two non-interacting quark propagators*. Assuming that the momentum of the probe is divided equally between the two propagators, then the appropriate momentum transfer in each propagator becomes $q/2$. Now, when going to the continuum limit, the denominators in (13) give the masses of the propagating particles as $1/2r_i^{\rm LE}$ i.e. in the charge case $am_{0,2\rm LE} = 0.36 \pm 0.02$ and $am_{1,2\rm LE} \approx 4.5$. Therefore, one interpretation of $m_{0,2\rm LE}$ is that this is the mass of a *constituent* quark used in the naive quark model description of the meson as simply two non-interacting quarks. This would give a vector mass of $am^v_{0,2\rm LE} = 0.72 \pm 0.04$. A similar interpretation can be made for the matter case to give a scalar meson of mass $am^s_{0,2\rm LE} = 1.07 \pm 0.05$.

It should be added that in our earlier work in [2] using the quenched approximation, the data were so sparse that an overall fit with only a single exponential was attempted over a limited range of r values – the overall fit with a single Yukawa being much worse. Therefore, to compare with the above values of $am^{v,s}$, a single Yukawa fit to the data at the largest values of r for which the data were still reliable was carried out. For case 3 in [2], the charge density data at $r = 3$ and 4 gave $am^v = 0.6(1)$ – scaled to $a = 0.14$ fm. Similarly, the matter density data at $r = 2$ and 3 gave $am^s = 1.0(2)$. These values are not significantly different to the present estimates.

In the above, the masses have been extracted by a somewhat tortuous argument. However, in the literature there have been direct calculations of the energies of these $q\bar{q}$ states using the same lattice parameters and lattice size as those employed here. In [3] they got $am^v_0 = 0.785 \pm 0.009$ and in [7] $am^s_0 = 1.18 \pm 0.08$. These numbers are consistent with our above estimates from the 2LE fit i.e. 0.72 ± 0.04 and 1.07 ± 0.05 respectively. Also from the 2LY fit, the scalar mass of $am^s_{0,2\rm LY} = 1.09 \pm 0.07$ is consistent with this value. But the vector mass of $am^v_{0,2\rm LY} = 0.56 \pm 0.02$ is somewhat too small. This difference can be considered as a measure of the systematic error on m^v_0 and suggests that the present data do not extend to sufficiently large values of r for a reliable estimate to be made of the asymptotic form.

Unfortunately, it is not straightforward to identify the above particles and their masses directly with physical particles, since we use light quarks that have the isotopic spin properties of u, d quarks but with masses about that of the strange quark. In addition, we do not calculate mass or density contributions that arise from disconnected correlations. For vector mesons, the latter has been shown in [13] to be only a small effect i.e. the OZI rule is justified in this case. On the other hand, this appears not to be so for scalar mesons. Evenso, in the vector case it is not reasonable to identify the above range of values $m^v_0 = 0.9 \pm 0.1$ and $m^v_1 = 1.4 \pm 0.3$ GeV directly with the isovector $\rho(0.77)$ and the radial excited $\rho(1.45)$ from [14], since in the quark model, the latter are constructed from u, d quarks with the correct mass – a value much less than the strange quark mass used here. However, since the OZI rule is a very good approximation for vector mesons, the additional mass of a state with strange quarks can be taken from the $\phi(1.02)$ meson – a value somewhat larger than our estimate of $m^v_0 = 0.9 \pm 0.1$ GeV. For the scalar mesons, the comparison with experiment is even more indirect. When comparing with our results, from [14] the appropriate states would be the $a_0(0.98)$ and $a_0(1.45)$, since our neglect of disconnected correlations effectively results in an isovector operator. However, as recently discussed in [15], these states probably have a complicated structure being mainly $(qq)_{\bar{3}}(\bar{q}\bar{q})_3$ in S-waves at short distances, with some $q\bar{q}$ in P-waves. But further out these rearrange into $(q\bar{q})_1(q\bar{q})_1$ and finally emerge as meson-meson states.

In fact this complication arises also in lattice calculations, since the present lattice parameters predict a pseudo-scalar meson (the "pion") with mass $am^{\rm ps} = 0.564$ – see Table 8 in [3]. This means that in Fig. 2 a cut in the T-direction can intersect *four* light-quark propagators – a state that can be interpreted as the exchange of two pseudo-scalar mesons. In the above scalar meson the $q\bar{q}$ are in a relative P-wave, so that it can couple to a two-meson state, where the mesons are in a relative S-wave. On the lattice such a two pseudo-scalar meson state would simply have a mass of $2am^{\rm ps} = 1.13$. This means that the scalar meson – calculated directly as a $q\bar{q}$ state with mass $am^s_0 = 1.18 \pm 0.08$ in [7] – is essentially degenerate with the two pseudo-scalar meson state and suggests that our estimate of, say, $am^s_{0,2\rm LY} = 1.09 \pm 0.07$ also contains this two-meson effect. It should be added that this problem does not arise for the vector meson, since there the $q\bar{q}$ are in a relative S-wave, so that the corresponding two-meson state has a relative P-wave leading to an energy considerably larger than $2am^{\rm ps} = 1.13$. This means that the structure of the vector meson generated here is expected to be mainly $q\bar{q}$ with little mixing with the two-meson state.

4.3.3 YS and LYS

The above considers directly the charge density. However, a similar analysis can be carried out on the $y_1(r)$, when the charge density is expressed in the separable form $x^{11}(r) = y_1(r)y_1(r)$. Since the single form fits ES, GS, LES and LGS

are given directly by their non-separable counterparts, as is clear by the relationships $a_0^{\rm F} \approx (a_0^{\rm FS})^2$, $r_0^{\rm ES} \approx 2r_0^{\rm E}$ and $r_0^{\rm GS} \approx \sqrt{2} r_0^{\rm G}$, they would add nothing new. The same is essentially true of the 2ES, 2GS, 2LES and 2LGS fits in Table 7, since the values of the $r_0^{\rm FS/LFS}$ and $r_0^{\rm 2FS/2LFS}$ are very similar. However, if the $y_1(r)$ are thought of as one of the two propagators in Fig. 2, then it is now appropriate to identify $y_1(r)$ with the YS and LYS forms. From Table 7 we get that $m_{0,\rm 2LYS} = 0.49 \pm 0.02$ and $m_{1,\rm 2LYS} = 0.58 \pm 0.02$ GeV.

This value of $m_{0,\rm 2LYS}$ is consistent with the earlier $m_{0,\rm 2LE} = 0.51 \pm 0.03$ GeV and supports the identification that these two very different ways of analysing the data are indeed extracting the propagator of the same "particle" and, as said above, it is tempting to identify this "particle" with a constituent quark. Since the density in the 2LE case can be expressed schematically in terms of two Yukawas (Y_i) as $Y_0Y_0 + Y_1Y_1$ compared with the corresponding expression in the 2LYS case $(Y_0' + Y_1')^2$, it is really only justified to compare the dominant terms Y_0Y_0 and $(Y_0')^2$.

In Table 8 we show the corresponding fits to the matter distribution giving $m_{0,\rm 2LYS} = 0.63 \pm 0.05$ and $m_{1,\rm 2LYS} = 1.0 \pm 0.2$ GeV. *If* these are now interpreted as the masses of constituent quarks, then scalar mesons constructed from two such *non-interacting* quarks – as in the naive quark model – would predict $m_0^s = 1.26 \pm 0.10$ and $m_1^s = 2.0 \pm 0.4$ GeV. The latter is consistent with $m_1^s(\rm 2LY) = 2.0 \pm 0.3$ GeV discussed earlier. However, the value of m_0^s is distinctly smaller than the earlier $m_0^s(\rm 2LY) = 1.53 \pm 0.09$ GeV and supports the point of view that scalar mesons cannot be described by the naive constituent quark model.

4.3.4 GS and LGS

The above Yukawa and exponential forms arise naturally in quantum field theory, whereas gaussians do not. However, when – as in [2] – an attempt is made to understand the densities in terms of solutions of the Dirac equation, it would be difficult to reconcile an exponential or Yukawa asymptotic tail with the usual form of linearly rising confining potential cr. When such a potential is introduced as a scalar potential, the solutions of the Dirac equation are asymptotically gaussian. This is most easily seen when – in the notation of [16] – the coupled Dirac equations for large r are written as

$$\begin{cases} G'(r) = m(r)F(r) \\ F'(r) = m(r)G(r) \end{cases}, \text{ giving } G'' - (cr)^2 G = 0, \qquad (18)$$

where $m(r) = m + cr \to cr$. The functions G and F are, therefore, seen to decay asymptotically as gaussians. Of course, the concept of a linearly rising confining potential does not hold for sufficiently large r, since eventually this will be quenched by the creation of $q\bar{q}$ pairs. Unfortunately, the actual demonstration of this unavoidable effect has yet to be achieved in a completely convincing manner for full QCD. However, the indications are that this will only occur for some value of r greater than about 1.2 fm, which – with the present lattice spacing of $a \approx 0.14$ fm – corresponds to a distance of almost $10a$. Therefore, in the range of interest here ($4a < r < 7a$) the linearly rising potential is still expected to be important and its repulsion could well suppress the density from being an exponential decay to more like a gaussian decay.

Support for a Dirac equation description is also given by our result that the charge and matter distributions are different – a feature not easy to understand in a non-relativistic approach. In the notation of (18) the charge and matter distributions can be expressed as

$$x_c^{\alpha\beta}(r) = G_\alpha(r)G_\beta(r) + F_\alpha(r)F_\beta(r) \quad \text{and}$$
$$x_m^{\alpha\beta}(r) = G_\alpha(r)G_\beta(r) - F_\alpha(r)F_\beta(r),$$

respectively. Attempts are now underway to study to what extent the above distributions can indeed be interpreted in terms of solutions (G, F) of the Dirac equation [17].

Our use, in Sect. 3.2, of the separable approximation when analysing the data was suggested by the form of the three-point correlation function C_3. The above interpretation of the data in terms of Dirac wavefunctions is consistent with this – namely – for small r the lattice data gives $x_c^{11} \approx x_m^{11}$. This implies that $G_1(r) \gg F_1(r)$ and both densities are approximately described by $G_1(r)G_1(r)$ – a separable form. On the other hand, at the largest values of r studied here, we get $x_c^{11} \approx 3x_m^{11}$ – implying that $G_1^2(r) \approx 2F_1^2(r)$ and so destroying the simple separability of the densities.

4.4 More on the charge sum rule

Comparing the values of the sum rule in Table 4, where the estimates are made by directly summing over all the lattice as in Sect. 3.3, and the values of $I^{\rm F}$ in Table 5, where they are made by summing the separate contributions from each vertex (x, y, z), we see that the latter in the 2LY case can be as large as 1.7(3) – a number that seems to be slightly larger than the direct sum of about 1.4(1). Of course, within the quoted error bars these two estimates agree. Even so there are reasons – to be discussed below – why exact agreement is not necessary. Firstly, it must be remembered that the direct estimate includes contributions from the whole lattice i.e. upto values of $r = 8\sqrt{3}$, whereas the data for a given r is based on only 18 values extending upto almost $r = 6$. More explicitly, the fits using (12) and (13) are to data with $r < 6$ – the largest being $x = 5, y = 3, z = 0$. In fact, a more correct statement would be that the fits are mainly dictated by the data for $r \leq 4$, with the remaining data, which have relatively large error bars, playing more of a supportive than a decisive role. Therefore, there is no guarantee that the expressions based on (12) and (13) are a good representation beyond $r \approx 4$.

To test the importance of the density contributions from large values of r, the summation over $\mathbf{r}$ in (15) is carried out explicitly but truncated in two ways by introducing either a cubic cut-off (C) or a spherical cut-off (S).

Table 10. Estimates of the charge sum rule from the $\mathbf{k} = 0$ component of (15). The $\mathbf{r}$ summation is truncated in two ways – cubic(C) cut-off, where $|x|, |y|$ and $|z|$ are all $\leq r_c$ and the spherical(S) cut-off, where only values of x, y and z with $x^2 + y^2 + z^2 \leq r_c^2$ are kept in the summation. The columns labelled I^{2E} and I^{2Y} are the integrals from 0 to r_c of the functions 2E and 2Y in Table 5. The row labelled None means the $\mathbf{r}$ summation is over the whole L^3 lattice

	2LE+data		2E	2LY+data		2Y
r_c	C	S	I^{2E}	C	S	I^{2Y}
3	0.95	0.62	0.63	0.95	0.62	0.58
4	1.20	0.87	0.90	1.20	0.87	0.85
5	1.37	1.11	1.10	1.38	1.11	1.06
6	1.49	1.30	1.23	1.51	1.30	1.21
7	1.58	1.42	1.31	1.61	1.42	1.37
None	1.62	1.62	1.6(3)	1.65	1.65	1.6(5)

In the cubic case, the x, y and z sums are each limited to the range $-r_c$to $+ r_c$, where r_c takes on values ranging from 3 to 7. The first values of r_c cover much of the range over which (12) and (13) were used to fit the data, whereas by going to $r_c = 7$ additional points are included that are outside this range. In the spherical cut-off, only values of x, y and z with $x^2 + y^2 + z^2 \leq r_c^2$ are kept in the summation. The outcome as seen in Table 10 shows several points:

1) There is little difference between the use of two lattice exponentials (2LE) versus two lattice Yukawas (2LY). This shows that, for the sum rule, the two forms are not only very similar at those values of (x, y, z) for which there exists lattice data but also at all other points on the lattice. Of course, when the expressions in (12) and (13) are used over the whole lattice, there is no need to resort to the explicit summation in (16), since the result (17) is known. However, it did serve as a numerical check.
2) The effect of including – where ever possible from Table 2 – the 18 actual lattice data points instead of the fitted forms has the minor effect of decreasing the sums by about 0.02. This is yet another reflection that the fitted forms are a good representation of the lattice data. Of course, these 18 points are only a small fraction of the total data needed in (15). Fortunately, about one half of the sum rule comes from contributions within a volume where $r \leq 3$ and these have all been measured directly.
3) The effect of using the Cubic (C)- versus the Spherical (S)-cutoff is large, with the latter being consistently about 0.2 smaller. This is natural, since for the same value of r_c the C-cutoff embraces more lattice points.
4) However, the most significant point is that the sums continue to increase significantly as r_c goes beyond the range where the lattice data is measured – with the value at $r_c = 5$ for the S(C)-cutoff being about 1.1(1.4) increasing to 1.4(1.6) at $r_c = 7$.

Table 11. This is a continuation of Table 10 for the spherical cutoff case (S) containing the available data. Here single exponential (E), Yukawa (Y) and gaussians (G) tails are included for $r > r_c$. The parameters of these tails are obtained from data with $r \geq 3$. The combined functions (2LE+E, 2LY+Y, 2LE+G and 2LY+G) are integrated using the cubic cutoff with $r = 7$

r_c	2LE+E	2LY+Y	2LE+G	2LY+G
3	1.42	1.46	1.30	1.30
4	1.40	1.45	1.28	1.28
5	1.41	1.46	1.29	1.29

The outcome is that, from the region $r \leq 4$, where the fits in (12) and (13) are most reliable, the contribution to the sum rule is about 1.2 – 1.4, which already is consistent with the direct summation estimate in Table 4. This, therefore, means that there is a significant contribution of about 0.4 – 0.5 coming from values of r greater than 4. In detail, a contribution of about 0.2 comes from the range $4 < r < 5$ and about 0.1 from the range $5 < r < 6$, where the fits seem to be supported by the data. The remaining discrepancy of almost 0.2 then comes from the periphery with $r \geq 6$, where there is no data to check the meaningfulness of the fits.

It, therefore, seems that the direct sum rule in Table 4 could well be slightly smaller that the explicit sum in (15). This possible difference can be interpreted in two ways: The explicit sum is an overestimate or the direct sum is an underestimate.

1) The fits using the expressions in (12) and (13) may indeed give a good fit to the data upto $r \approx 4$, but are *not* good estimates of the poor and missing data for $r > 4$. To test this, the lattice forms 2LE and 2LY are used upto $r = r_c$ and the single non-lattice forms based on 2E, 2Y and 2G in Table 5 are used for $r > r_c$. The outcome is shown in Table 11. As expected the combinations 2LE+E and 2LY+Y give results in the range 1.4–1.5, which are close to those of the spherical cutoff with $r_c = 7$ in Table 10. On the other hand, the combinations 2LE+G and 2LY+G – containing the gaussian tail – give a result of ≈ 1.3, which is noticeably smaller than the 2LE+E or 2LY+Y numbers. Furthermore, all of these combinations result in sum rules that are smaller than the $r_c = 7$ *cubic* cutoff values of almost 1.7.
2) The second – and less likely – interpretation is that the fits with Yukawa and exponential forms do indeed give a good estimate of the poor and missing data for $r > 4$. This would mean that the values of the sum rules in Table 4 are an underestimate and that the measured contributions there from $r > 4$ are too small. An example of this will be seen later in Table 12 of the next subsection. There the three-point correlation function for $r = 5$ is consistent with that for $(x = 3, y = 4)$ for $T \leq 6$ – but with errors that are twice as big. However, for $T > 6$ – the T range necessary for extracting densities – the signals from the two cases differ greatly, with those for $r = 5$ simply disappearing. Possibly sim-

Table 12. Check on the rotation invariance of $R(r) = \langle C_{3,\mathrm{F_1F_1}}(T,r)\rangle/\langle C_{2,\mathrm{F_1F_1}}(T)\rangle$ for $r = 3$ versus $x = 2, y = 2, z = 1$ and $r = 5$ versus $x = 3, y = 4$. All entries should be multiplied by 10^{-4}

T	$R(r=3)$	$R(2,2,1)$	$R(r=5)$	$R(3,4)$
4	23.0(4)	11.6(2)	1.2(4)	1.2(2)
5	24.4(4)	13.4(3)	1.7(4)	1.6(2)
6	25.4(6)	15.3(4)	2.0(5)	2.2(3)
7	25.7(7)	16.2(4)	1.1(6)	2.8(3)
8	26.2(1.1)	17.7(0.7)	0.8(9)	3.9(5)
9	26.8(1.5)	17.4(0.9)	1.0(1.2)	5.0(7)
10	28.8(2.7)	17.4(1.5)	2.9(2.2)	7.0(1.3)

ilar underestimates could occur for larger values of r, where the fits from (12) and (13) suggest a significant contribution (≈ 0.3) to the sum rule should arise. However, this would be surprising since it is not usual for there to be such systematic trends. Normally in such cases, one would expect the results to fluctuate from being too low for some values of r to being too high at others. However, if the trend suggested by the $r = 5$ data were true then this would mean that the charge sum rule could be larger than that measured directly – possibly upto about 1.7. Unfortunately, to now get the value of unity expected in the continuum limit, would then require a vertex renormalisation factor of about $1/1.7 \approx 0.6$ – a number significantly smaller than the estimates in [11].

The first interpretation has two nice features. Firstly, with a charge sum rule of about 1.3, the required vertex renormalisation factor to ensure unity in the continuum would be about 0.8 – a value more in line with the estimates in [11]. Secondly, when – as in [2] and discussed above – an attempt is made to understand the charge density in terms of solutions of the Dirac equation, exponential and Yukawa forms do not arise naturally, whereas gaussian forms do as illustrated in (18).

For the matter sum rule we saw in Table 4 that 0.9(1) was a reasonable compromise. The predictions using the algebraic fits are shown as I_{F} in Table 6 and are seen to have much larger error bars than their charge counterparts. All that can be said is that the I^{F}'s are – within these large uncertainties – consistent with the direct measurement of 0.9(1).

The conclusion from this section is not definite. If the asymptotic form of the density is indeed exponential or Yukawa, then the charge sum rule is 1.4 to 1.5. However, it is not possible to rule out an asymptotic form that is gaussian. In that case the charge sum rule could be less than 1.3.

4.5 Rotational invariance

Since off-axis points are considered, in principle it should be possible to check rotational invariance. In particular, comparisons between the on-axis point $r = 5$ and the off-axis point $(x, y) = (3, 4)$ data and also the $r = 3$ and $(x, y, z) = (2, 2, 1)$ data are of special interest. In Table 12 the ratios $\langle C_{3,\mathrm{F_1F_1}}(T,r)\rangle/\langle C_{2,\mathrm{F_1F_1}}(T)\rangle$ are shown for the dominant charge correlation. This table shows several points:

1) The $r = 3$ and $(2, 2, 1)$ data both have good signals for all values of T. This shows clearly that rotational invariance is violated with $x^{11}_{\mathrm{F_1F_1}}(r = 3)$ being almost twice $x^{11}_{\mathrm{F_1F_1}}(2, 2, 1)$. The reason for this lack of rotational invariance in such an extreme off-axis case could be due to the presence of the single $z = 1$ step in $(2, 2, 1)$. A similar effect can be seen in Fig. 3 for the $(1, 1, 1)$ data which is also lower than the general trend. For less extreme cases such as $(2, 1)$, rotational invariance seems to be better satisfied.
2) The $r = 5$ signal disappears at $T = 7$ - rendering it useless to extract the density, since this requires reliable data for $T > 7$. This negative result is anyhow of interest, because in [2] $r = 5$ was the largest value of r analysed and it suggested that the charge density was considerably smaller than would be expected from a simple exponential dependence. This is no longer the case.
3) The $(x, y) = (3, 4)$ signal is good for all T. This improvement over the $r = 5$ case is presumably due to the fact that each off-axis correlation is measured 24 times compared with the 6 on-axis measurements.
4) For $T < 7$, the two sets of data are in agreement, as would be expected if rotational invariance had been achieved. However for $T \geq 7$, the $C_3(r = 5)$ signal essentially disappears.

Table 13. Lack of rotation invariance in the lattice Yukawa and exponential forms in (12) and (13) for $r = 3$ versus $(x, y, z) = (2, 2, 1)$ and $r = 5$ versus $(x, y) = (3, 4)$

Case	$r = 3$	$(2,2,1)$	Ratio
2LY(Table 5)	0.002893	0.002566	0.89
2LE(Table 5)	0.002893	0.002573	0.89
	$r = 5$	$(3,4)$	Ratio
2LY(Table 5)	0.000709	0.000653	0.92
2LE(Table 5)	0.000706	0.000651	0.92

If the lattice Yukawa and exponential forms in Sect. 4 are used to estimate the rotational invariance, we get the results in Table 13. Both forms give the same results well within 1%. However, for the two cases considered involving directly the lattice data – $r = 3$ versus $(2, 2, 1)$ and $r = 5$ versus $(3, 4)$ – the off-axis values are about 10% less than the corresponding on-axis value. For $r = 3$ versus $(2, 2, 1)$ this difference is considerably smaller than the actual lattice data requires. On the other hand, for $r = 5$ versus $(3, 4)$ the reverse could be true with the difference being much larger than is suggested by the small T values in Table 12.

It should be added that this study of the $(2, 2, 1)$ case was only carried out after the bulk of this work was com-

pleted. In particular, the (2,2,1) data was *not* included in the fitting that led to the exponential, Yukawa and Gaussian parameters in Tables 5 to 8. However, its direct inclusion did not result in values of the a_i and r_i that were outside of the error bars given in Tables 5 to 8, even-though each $\chi^2/n_{\rm dof}$ did increase by about 0.3 – 0.4. A more realistic way to treat this data is to combine the $r = 3$ data with that for (2,2,1) using the relative weights of 6 to 24 – the number of equivalent possibilities for the two cases. When this weighting is also used for the fitting functions, the $\chi^2/n_{\rm dof}$ decreases slightly from the values in Tables 5 to 8. However, again the final values of the a_i and r_i are unchanged within the errors quoted. This suggests that the overall fits are sufficiently stable that the effect of any particular case may lead to a large χ^2 contribution for that case but still leave the fit essentially unchanged. It should be noted that the $r = 3$ and $(2, 2, 1)$ charge data only differ by about two standard deviations, so that the above problem could even evaporate if more gauge configurations were used.

5 Conclusion

In this paper charge (vector) and matter (scalar) radial distributions have been measured on a lattice for the heavy-light meson $(Q\bar{q})$, where Q is a static quark and $\bar{q}$ has a mass approximately that of the strange quark. The charge distribution could be determined reasonably well upto an interquark distance of about 6 lattice spacings i.e. $\approx$ 0.8 fm. In comparison, matter distribution measurements could only be carried out upto about 4 lattice spacings i.e. $\approx$ 0.6 fm. The drop-off of the charge distribution can be well described by the exchange of a vector meson of mass $\approx$ 1 GeV. On the other hand, the drop-off of the matter distribution is described by the exchange of an scalar meson of mass $\approx$ 1.5 GeV.

In the conclusion of [2] several refinements and extensions to that pilot calculation of charge and matter distributions were listed. Here we have carried out a few of these:

1) Probably the most important "refinement" is the replacement of the quenched approximation by the use of dynamical fermions. However, as seen in Fig. 3, we find that the two appear to be indistinguishable within the accuracy of the present work. In [9] and [10] it was suggested that in the matter distribution there could be a difference due to the presence of disconnected quark-loop contributions. The fact that this is not seen here could be due to our use of sea quarks that have a mass about that of the strange quark mass.
2) Radial correlations at off-axis points are now measured. This meant that the number of data points accessible before the noise takes over is much larger – going from about 6 to 18. This enables us to achieve better algebraic fits to the data. However, one of our hopes, to see rotational invariance by comparing the data for $r = 5$ and $(3, 4)$ was only partially successful – see Table 12.
3) The lattice spacing is now smaller – 0.14 fm compared with the earlier 0.17 fm. Also the number of gauge configurations is larger – 78 versus 20 earlier.

However, the list in [2] contained other points not touched here:

1) So far we have only extracted S-wave correlations. We still need to measure the $P_{1/2}$, $P_{3/2}$, $D_{3/2}$, $D_{5/2}$, ... densities corresponding to the energies extracted in [5]. Also for a given orbital angular momentum, do these correlations show the degeneracy predicted in [18]?
2) The measurement of correlations in the baryonic and $(Q^2\bar{q}^2)$ systems. Are these similar to those in the $(Q\bar{q})$ system – as is the case when comparing correlations in few-*nucleon* systems? If this is so, then it would encourage phenomenological approaches such as that mentioned above utilizing the Dirac equation.
3) As with all lattice calculations, there is the need to check the continuum limit by using finer and larger lattices. The former has, to some extent, been checked by the comparison between our earlier work in [2] with $a = 0.17$ fm and this study with $a = 0.14$ fm. There, as seen in Fig. 3, the two sets of results agree after scaling. However, the two calculations also differ by their use of quenched versus unquenched gauge configurations. A more correct comparison would involve the use of the same type of configurations – quenched or unquenched. Even so, our present comparison – in spite of its failings – is encouraging.
4) So far we have dealt with light quarks (valence and sea) that have the isospin form of u, d quarks but with a mass about that of the strange quark and heavy quarks that are static. The use of such quark masses means that the nearest physical meson with which we can possibly compare our calculations is the $B_{\rm s}(5.37\ {\rm GeV})$. However, for a more realistic comparison we should eventually have a heavy quark with mass about 5 GeV and u, d quarks with their correct mass.
5) In this work we have only probed the charge and matter distributions using the γ_4 and unity probes. However, other probes are possible such as: i) The pseudo-vector operator $(\gamma_\mu\gamma_5)$ needed for the $B^*B\pi$ coupling – see [19]; ii) Probes to study the color structure of the gluon fields and possible $q\bar{q}$ condensates surrounding the $Q\bar{q}$ system.

This study is now at the stage where we have the energies and the corresponding charge and matter radial distributions for the ground and first excited S-wave states. In the future we hope to have these quantities for the other partial waves in [5]. These results can possibly be utilized in at least two ways:

1) When, for example, calculating electromagnetic transitions between different $Q\bar{q}$ states the form of the transition matrix elements could be guided by the above radial distributions.
2) As discussed in the Introduction – and also as partial motivation for the separable method for analysing the lattice data – the radial distributions could be interpreted in terms of wavefunctions. This would mean we

are in the position of having some of the eigenvalues and eigenfunctions of an Hamiltonian, whose form we do not know. We are then at liberty to find this Hamiltonian to construct an effective theory. This effective Hamiltonian could be, for example, of Schroedinger or Dirac form with suitable interactions. As discussed in Sect. 4.3, the latter form is probably more appropriate, since the charge and matter distributions are different – a feature not easy to understand in a non-relativistic approach.

This study has shown that – using lattice techniques – reliable estimates can be made not only of spectra but also of wavefunction information. This is just the beginning – with future studies expected to enlarge this information and also to attempt interpretations outside of quantum field theory.

Acknowledgements. The authors wish to thank the Center for Scientific Computing in Espoo, Finland for making available computer resources without which this project could not have been carried out. One of the authors (J.K.) also wishes to thank the Magnus Ehrnrooth Foundation for financial support. Useful conversations with Nils Törnqvist are also acknowledged.

References

1. C. Gobbi, F. Iachello, D. Kusnezov, Phys. Rev. D **50**, 2048 (1994)
2. A.M. Green, J. Koponen, P. Pennanen, C. Michael, Phys. Rev. D **65**, 014512 (2002), hep-lat/0105027
3. UKQCD Collaboration, C.R.Allton et al., Phys. Rev. D **60**, 034507 (1999), hep-lat/9808016
4. UKQCD Collaboration, C. McNeile, C. Michael, Phys. Lett. B, **491**, 123 (2000), hep-lat/0006020
5. C. Michael, J. Peisa, Phys. Rev. D **58**, 034506 (1998), hep-lat/9802015
6. A.M. Green, C. Michael, J.E. Paton, Nucl. Phys. A **554**, 701 (1993), hep-lat/9209019
7. UKQCD Collaboration, C. McNeile, C. Michael, Phys. Rev. D **63**, 114503 (2001) hep-lat/0010019
8. A.M. Green, J. Lukkarinen, P. Pennanen, C. Michael, Phys. Rev. D **53**, 261 (1996); J. Lukkarinen, Extracting Four-Quark Binding Energies from Lattice Monte Carlo Data, MSc thesis, Helsinki 1996
9. UKQCD Collaboration, M. Foster, C. Michael, Phys. Rev. D **59**, 074503 (1999), hep-lat/9810021
10. M. Foster, University of Liverpool PhD thesis 1998
11. K.C. Bowler, L. Del Debbio, J.M. Flynn, G.N. Lacagnina, V.I. Lesk, C.M. Maynard, D.G. Richards, Nucl. Phys. B **619**, 507 (2001), hep-lat/0007020; A.A. Khan et al. CP-PACS, Phys. Rev. D **65**, 054505 (2002), hep-lat/0105015; S. Aoki et al. CP-PACS, Nucl. Phys. Proc. Suppl. **106**, 780 (2002), hep-lat/0110128
12. C.B. Lang, C. Rebbi, Phys. Lett. B **115**, 137 (1982)
13. UKQCD Collaboration, C. McNeile, C. Michael, K.J. Sharkey, Phys. Rev. D **65**, 014508 (2001)
14. D.E. Groom et al., Eur. J. Phys. C **15**,1 (2000)
15. F. Close, N. Törnqvist, J.Phys. G **28**, R249-R267 (2002), hep-ph/0204205
16. J.D. Bjorken, S.D. Drell, Relativistic Quantum Mechanics (McGraw-Hill, Inc., 1964)
17. A.M. Green, J. Ignatius, M. Jahma, J. Koponen, work in progress
18. P.R. Page, T. Goldman, J. N. Ginocchio, Phys. Rev. Lett. **86**, 204 (2001), hep-ph/0002094
19. G.M. de Divitiis, L. Del Debbio, M. Di Pierro, J.M. Flynn, C. Michael, J. Peisa, JHEP 9810:010 (1998), hep-lat/9807032